Calibration and data quality of warm IRAC

S. J. Carey*[a], J. A. Surace[a], W. J. Glaccum[a], J. Ingalls[a], J. Krick[a], M. Lacy[a,b], P. Lowrance[a], S. Laine[a], J. O'Linger[a], J. R. Stauffer[a], S. P. Willner,[c] J. L. Hora[c], W. F. Hoffmann[d], M. L. N. Ashby[c], J.-S. Huang[c], M. Maregno[c,e], M. Pahre[c], Z.Wang[c], M. Werner[f], G. G. Fazio[c]

[a]Spitzer Science Center, MS 220-6, California Institute of Technology, Pasadena, CA, USA, 91125;
[b]National Radio Astronomy Observatory, 520 Edgemont Road, Charlottesville, VA, USA, 22903;
[c]Harvard-Smithsonian Center for Astrophysics, 60 Garden Street, Cambridge, MA, USA, 02138;
[d]Steward Observatory, 933 N. Cherry Avenue, Tucson, AZ, USA, 85721;
[e]Iowa State University, A313E Zaffarano, Ames, IA, USA, 50011;
[f]Jet Propulsion Laboratory, 4800 Oak Grove Drive, Pasadena, CA, USA, 91109

ABSTRACT

We present an overview of the calibration and properties of data from the IRAC instrument aboard the *Spitzer* Space Telescope taken after the depletion of cryogen. The cryogen depleted on 15 May 2009, and shortly afterward a two-month-long calibration and characterization campaign was conducted. The array temperature and bias setpoints were revised on 19 September 2009 to take advantage of lower than expected power dissipation by the instrument and to improve sensitivity. The final operating temperature of the arrays is 28.7 K, the applied bias across each detector is 500 mV and the equilibrium temperature of the instrument chamber is 27.55 K. The final sensitivities are essentially the same as the cryogenic mission with the 3.6 μm array being slightly less sensitive (10%) and the 4.5 μm array within 5% of the cryogenic sensitivity. The current absolute photometric uncertainties are 4% at 3.6 and 4.5 μm, and better than milli-mag photometry is achievable for long-stare photometric observations. With continued analysis, we expect the absolute calibration to improve to the cryogenic value of 3%. Warm IRAC operations fully support all science that was conducted in the cryogenic mission and all currently planned warm science projects (including Exploration Science programs). We expect that IRAC will continue to make ground-breaking discoveries in star formation, the nature of the early universe, and in our understanding of the properties of exoplanets.

Keywords: infrared detectors, space telescopes, *Spitzer* Space Telescope, IRAC

1. INTRODUCTION

The *Spitzer* Space Telescope[1] is the fourth of NASA's great observatories and has made paradigm-shifting discoveries using its three infrared instruments, the Multi-band Imaging Photometer for *Spitzer*[2] (MIPS), the Infrared Spectrometer[3] (IRS) and the InfraRed Array Camera[4,5] (IRAC), covering a wavelength range from 3.6 to 160 μm, during its 5.45 year primary mission. The duration of the primary mission plus the three month in-orbit checkout (5.7 years of cryogenic lifetime) far exceeded the goal mission lifetime of five years. The success of the passive cooling of *Spitzer* by using an Earth-trailing orbit and judicious use of the makeup heater, which evaporated cryogen to actively cool the telescope mirror to permit observations with the longest wavelength (MIPS and IRS) instruments, were key elements in the great length of the cryogenic mission.

Cryogen was finally exhausted on the *Spitzer* Space Telescope on 15 May 2009 during routine science observations. Once the cold assembly temperature limit of ~3 K, fault protection was invoked and *Spitzer* entered safe mode at 15 May 2009 22:11:27 UTC. Until safe mode entry, *Spitzer* was performing nominally and collecting quality science data. Figure 1 displays the raw data from the last cryogenic data collection, an IRAC observation of the photometric calibrator, NPM1 +68.0422. A companion paper[6] in this volume presents the absolute calibration of cryogenic IRAC data.

The remainder of this paper will deal with the operations of the IRAC instrument. IRAC consists of four 256 × 256

*carey@ipac.caltech.edu.com; phone 1 626-395-8796

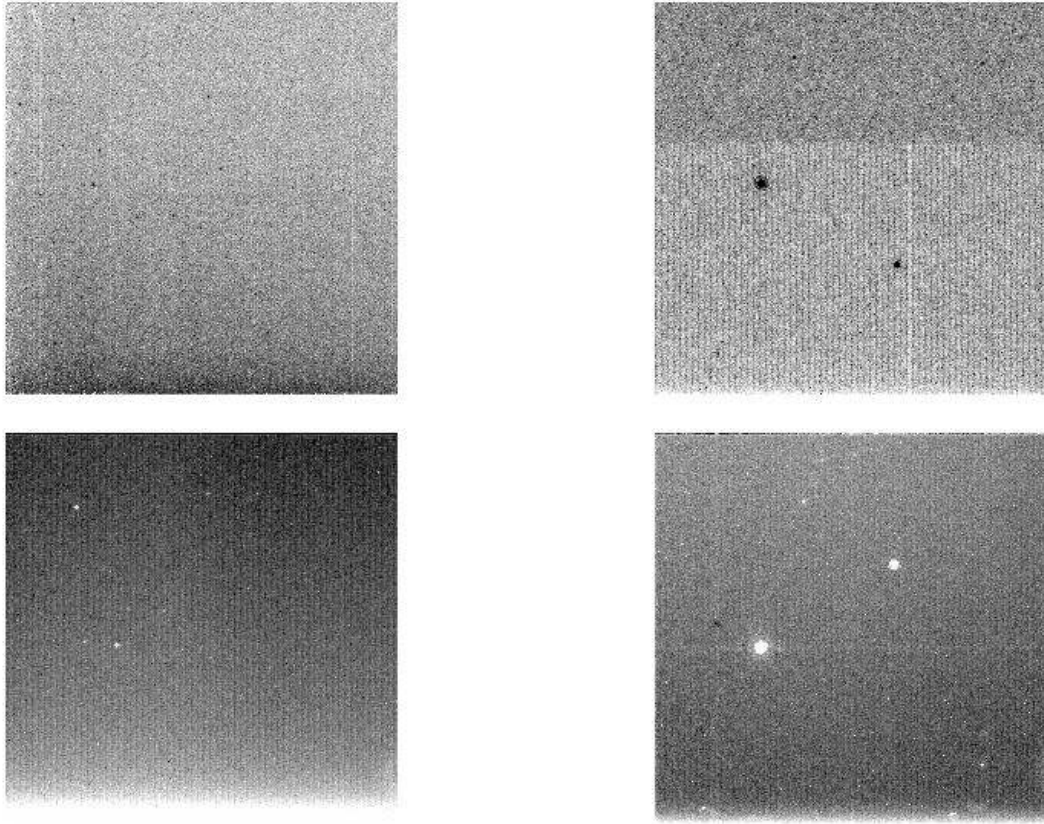Figure 1. Raw IRAC images at 3.6 (upper left), 4.5 (upper right), 5.8 (lower left) and 8.0 μm (lower right) of NPM1 +68.0422. These images are the last data taken with *Spitzer* before the safe mode entry ending the primary cryogenic mission. NPM1 +68.0422 is visible as the fainter of two sources in the 4.5 and 8.0 μm images. Note that in the raw frames the orientation of 4.5 and 8.0 μm images are reversed in the y direction.

arrays viewing two sets of 5.2 × 5.2 arcminute fields of view with broadband filters spanning 3-9 μm. The fields of view are slightly offset with a gap of ~1 arcminute between them with two pickoff mirrors feeding the IRAC optical system. Each field of view is imaged by one InSb array and one Si:As impurity band conduction (IBC) array. The passbands of the InSb arrays are centered on 3.6 and 4.5 μm, respectively. The IRAC focal planes are actively thermally controlled with temperatures stable to a few milli-Kelvin. This stability is achieved by heating the arrays using an active feedback thermal control using a proportional controller and Cernox sensors. Each array also has a diode temperature sensor used for determining the appropriate temperature range for the multiply valued Cernox sensors. The cryogenic operating temperatures are 15 K for the InSb and 6 K for the Si:As arrays. The array heaters can heat the InSb arrays to temperatures of ~40 K for superfluid baseplate temperatures. The arrays are read out using a set of four multiplexers for each channel. Each multiplexer reads one column at a time with four columns addressed at once. The arrays are read using non-destructive pairs of Fowler samples with the measured value being the average of the difference of the signal and pedestal pairs. During the five plus years of cryogenic operation, no degradation in image quality or array properties has been noted except for a slight increase in hot pixels for the 8.0 μm Si:As array[7].

Prior to the end of the cryogenic mission, it was noted that the passive cooling would continue to achieve telescope and multiple instrument chamber (MIC) temperatures of ~30 K. Thermal models assuming 3 mW of power for operating IRAC predicted MIC temperatures of between 25 and 29 K and primary mirror temperatures of 24-25 K. Due to the excellent thermal isolation of the telescope, it would take approximately two months to reach equilibrium. The thermal background of the telescope and the noise properties[8] of the two InSb arrays of IRAC for passively cooled *Spitzer* should provide comparable sensitivity to the cryogenic observations at 3.6 and 4.5 μm. A science case[9] for an extended mission (called the warm mission in the remainder of this article) using the shortest wavelength cameras of IRAC was prepared and a three year (initial two year plus one year extension) post-cryogenic extended mission was awarded by NASA.

2. INITIAL WARM CHARACTERIZATION

Before warm mission science observations could commence, the operating parameters of IRAC at ~30 K needed to be determined and optimized and initial calibrations analogous to the cryogenic ones during the initial in-orbit checkout and prior ground testing needed to be developed. The characterization at ~30 K was delayed for approximately one month to develop and implement a firmware patch to enable active temperature control between 25 and 33 K for the arrays. The firmware patch involved adjusting the Cernox control current to enable commanding control voltages permitted by the 12-bit nature of the digital-to-analog converter to produce the correct temperatures. During the development of the firmware patch, IRAC collected characterization data at temperatures between 22 and 28 K including a 72 hour observation of the GRB 090423[10]. The cryogenic bias settings were used for these observations. The noise properties of this observation are comparable to any deep imaging conducted in the cryogenic mission. Figure 2 displays the 3 sigma detection of the gamma-ray burst at 3.6 μm.

The initial characterization phase took place between 18 June and 28 July 2009. The characterization was complicated by uncertainties in the calibration of the temperature sensors and the slow warming trend of the MIC. Not unexpectedly, the characterization data demonstrated that the image noise increased with array temperature and decreased with applied bias. Noisy and unusable pixels increased with both array temperature and applied bias. As shown in Figure 3, the trends are more significant for the 3.6 μm array, while the noise properties of the 4.5 μm array are relatively insensitive to operating temperature. In addition, some array artifacts such as column pulldown were much more significant with increased temperature and for higher applied biases. Optical properties such as the array locations with respect to boresight, focus and array distortion maps did not change measurably from the cryogenic values.

Based on the initial and conservative assumptions about the equilibrium temperature of the MIC and power dissipated by IRAC and the need to heat the arrays to maintain active thermal control, the array temperatures were set to 31 K. The applied biases across each detector were set to 450 mV, the bias that both maximizes responsivity while keeping hot and noisy pixels to an acceptable value. In addition to the commandable array temperature, each array has five programmable biases: the array clamp, reset voltage (VRST), detector voltage (VDET, the applied bias across the detector is VDET-VRST), VGG1, which controls the amount of current through the unit cell source-follower amplifiers, and the drain voltage on the unit cell source-follower circuits (VDDUC). VRST was chosen to keep the pedestal levels on scale while permitting the largest dynamic range possible. In addition, the pedestal levels were more stable for lower VRST. VDDUC matched VRST, for VDDUC values different than VRST, the pedestal values were not stable. More positive VGG1 decreased noise levels; however, the pedestal levels were much less stable. VGG1 was chosen to minimize noise while keeping the bias pattern stable and maintaining the VSSI1 current at similar values to the cryogenic operations. VDET was chosen to provide the applied bias for a given VRST. The array clamps were used as in
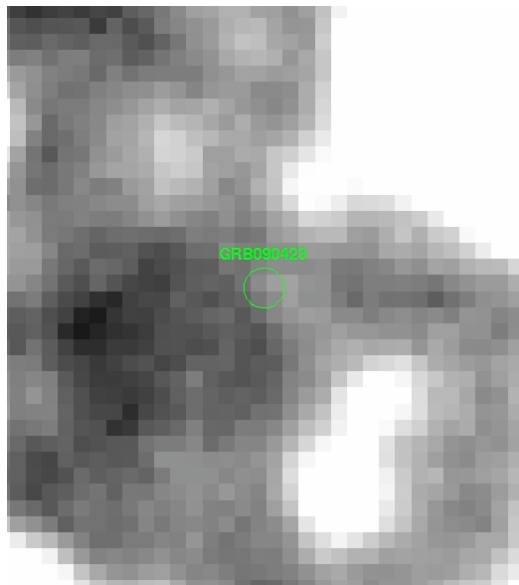

Figure 2. 3.6 μm detection of GRB 090423. The source is 46 nJy at 3.6 μm while the total noise in an equivalent aperture is 17 nJy.

the cryogenic mission. For the 3.6 μm array, the clamp remained broken at the higher operating temperatures and was not used. The initial characterization was conducted with the array parameters given in Table 1.

During the characterization, it was realized that the initial estimate for the MIC equilibrium temperature was too pessimistic in part as IRAC was dissipating 53% less power than estimated (1.4 mW actual, 3.0 mW estimated) as lower heater power was required to maintain thermal stability above the warmer baseplate. Revised thermal modeling indicated that at ~30 K, IRAC was the major heat input to the MIC, heating the MIC by 1.2 K per mW of power dissipated. At 3.6 μm, operating at a lower temperature dramatically reduces the image noise as shown in Fig. 3. In addition, by operating at a lower temperature the number of noisy pixels for a given applied bias is decreased permitting the use of higher applied biases and greater responsivity.

The IRAC array heaters were commanded off 12 August 2009 to allow the MIC to cool as the best equilibrium temperature had been slightly overshot. On 18 September 2009, the final warm setpoints were commanded and the array temperatures actively controlled. Table 1 provides the parameters for the three phases of the warm mission, 1) array temperatures = 31 K and applied bias of 450 mV, 2) array temperatures floating from 29 K to 28.5 K and applied bias of 450 mV, 3) array temperatures actively controlled to 28.7 K and applied bias of 500 mV. Each of the three phases has a

Table 1. Commanded array parameters, 3.6/4.5 μm.

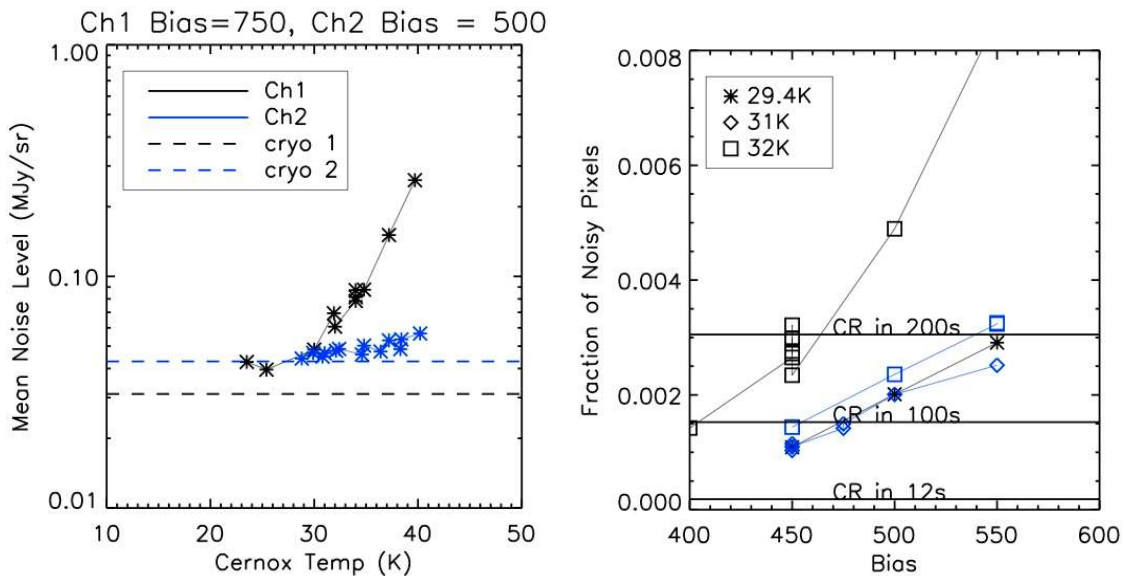| Phase	T	VDET	VRST	VGG1	VDDUC	Clamp
	Kelvin	Volts	Volts	Volts	Volts	
Initial characterization	31 / 31	-3.15/-3.10	-3.60/-3.55	-3.685/-3.610	-3.60/-3.55	OFF/ON
MIC cooling	29-28.5/29-28.5	-3.15/-3.10	-3.60/-3.55	-3.685/-3.610	-3.60/-3.55	OFF/ON
Final setpoints	28.70/28.67	-3.10/-3.05	-3.60/-3.55	-3.685/-3.610	-3.60/-3.55	OFF/ON
Cryogenic	15/15	-2.75/-3.50	-3.50/-3.50	-3.65/-3.65	-3.50/-3.50	OFF/ON

Figure 3. Variation of noise (left) and number of noisy pixels (right) as a function of array temperature (and bias for the noisy pixel fraction) for the 3.6 (black) and 4.5 μm (blue/grey) arrays using the cryogenic applied biases of 750 and 500 mV, respectively. The cryogenic noise values are shown by dashed lines. Lines showing the fraction of pixels affected by radiation hits for frametimes of 12, 100 and 200 seconds are shown in the right hand panel.

Table 2. Flux conversions for the phases of the warm mission. The flux conversions for the initial characterization and MIC cooling stages have been corrected for the normalization of pixel-phase effect by 4% and 2% at 3.6 and 4.5 μm.

Phase	Dates	FLUXCONV (MJy/sr) / (DN/s)	
		3.6 μm	4.5 μm
Initial characterization (1)	18 June -12 August 2009	0.1333	0.1489
MIC cooling (2)	12 August – 18 September 2009	0.1306	0.1479
Final setpoints (3)	18 September onward	0.1253	0.1469
Cryogenic		0.1088	0.1388

different absolute flux conversion and uses skydarks taken with those array settings to remove array biases from the calibrated data. A complete set of calibrations was only created for phase 1) and phase 3). For the floating temperature phase, the non-linearity solution and flat-field applied are the same as the original characterization data. The phase 2) data have greater uncertainty in their calibration as the phase 1) calibrations do not strictly apply. The linearity solution for phases 1) and 2) is not currently optimal. As a result, the absolute calibration is uncertain by 5-7% for 3.6 μm sources brighter than 1/3 full well and 5% for faint sources at 3.6 μm and all sources at 4.5 μm. During the MIC cooling, the flux conversion was measured by observing the IRAC primary calibrators every week. Despite the temperature change on the arrays, the flux conversion varied by less than our ability to measure it during this time span, that is, temperature variations in the flux conversions were less than 1%.

Several modifications to data taking were implemented as part of the warm mission. A 2 second subarray frametime was added to facilitate long term staring observations of exoplanets. To mitigate anticipated high readnoise, 200 and 400 second Fowler frames were tested, but it was determined that they provided no sensitivity benefit compared to comparable observations using 100 second frametimes. As the longer frametimes significantly increase the calibration budget, they were dropped for efficiency. The 12 and 30 second frametimes had the number of Fowler samples increased from 16 to 32 at 3.6 μm to improve sensitivities for extragalactic shallow surveys. The Fowler sampling for the 0.4 second subarray observations was decreased to maximize effective integration time and signal-to-noise for bright source observations.
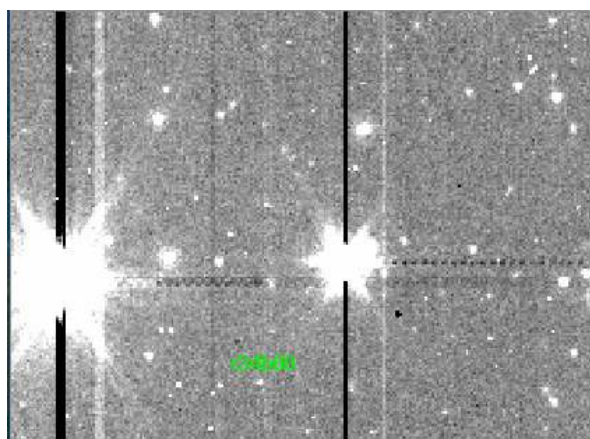

Figure 4. Example of negative muxbleed seen in 4.5 μm data taken at a temperature of 24.3 K. Also seen are strong column pulldown (dark vertical stripes) and column pulldown residuals (bright stripes produced by column pulldown in the previous frame).

Minor revisions were made to the IRAC data processing pipeline. Currently, no lab darks are subtracted from warm data as no ground calibrations exist. As a result, the history dependent bias variation (also known as the "first-frame" effect) is not removed from warm data. The muxbleed correction has been turned off in the warm pipeline as the effect is not

seen in IRAC data taken above 25 K. Muxbleed is an image artifact that manifests itself as a trail of decaying but bright pixels for a given multiplexer after that multiplexer observes a sufficiently bright source. Muxbleed is believed to be due to residual charge decay in the multiplexer. In characterization data at ~23 K, the muxbleed exhibited very complicated behavior and was a strong function of applied bias on the array. In some instances, the muxbleed was negative as shown in Figure 4.

A complete recalibration for phase 3) was conducted from 23 September to 02 October 2009. The recalibration was of shorter duration that the initial characterization as the array parameters were already set and most optical properties such as focus and distortion had already been mapped sufficiently. However, a complete point response function map was made as that depends significantly on the linearity solution. The remainder of this paper describes the properties of warm IRAC data after the final setpoint determination.

3. PROPERTIES OF WARM MISSION DATA

We compare and contrast the quality and properties of warm IRAC data to data from the cryogenic mission. In general, the data are very similar to the cryogenic and the optical properties such as image noise pixels are indistinguishable. The lack of optical property change is not unexpected as the expected linear expansion in materials in the optical path is expected to be less that a part in 10^{-5} at these temperatures. Variations in the calibrations applied such as bias (dark) subtraction, linearity solution and flat-field are compared. Note that while the calibrations are different and in some cases more extreme for warm data, the data are still calibrated to the same level of accuracy and the images produced by the Spitzer Science Center pipeline are science quality.

3.1 Bias

The bias of the Fowler sampled data has increased significantly from the cryogenic data. Figure 5 displays representative skydark measurements from the cryogenic and warm missions. As in the cryogenic mission, the bias increases with frametime but does not scale linearly with frametime. The dark currents in the warm mission are estimated to be below one electron per second for both arrays, but this quantity is difficult to measure without use of the IRAC shutter. In addition to more significant DC bias levels, there is increased structure in the dark frames which manifest as vertical striping in the images. The structure now masks the pixel-to-pixel scatter in the bias. The faint horizontal features in the 4.5 μm darks are also apparent but just barely in the cryogenic versions. For the 3.6 μm array, there are also more hot columns of pixels (dark columns in Fig 5.). Despite the bias being more significant, it is stable and reliably removed using the standard IRAC pipeline. For warm observations, the bias is subtracted using skydark calibrations taken every week. The nearest in time skydark is selected and subtracted from any given observation.
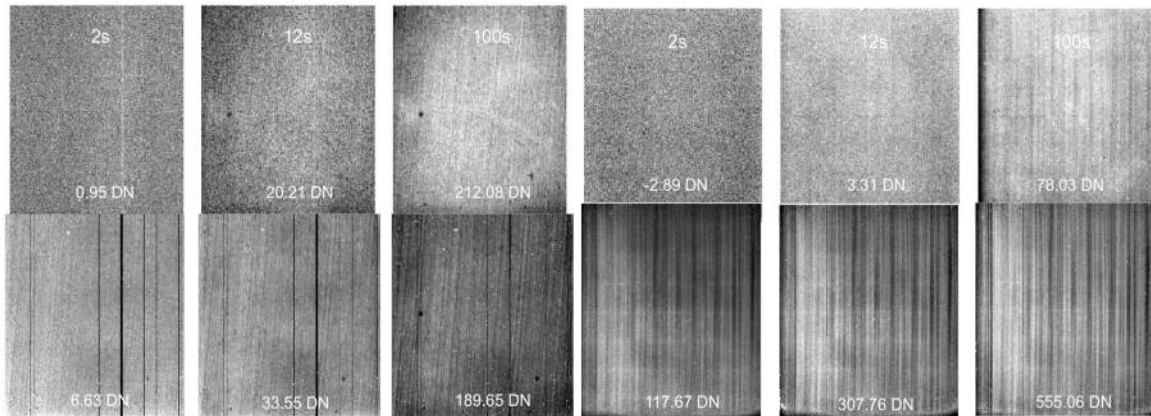

Figure 5. The Fowler bias as measured using observations of a standard field at high Ecliptic latitude at 3.6 μm (left set of six figures) and 4.5 μm (right set). The cryogenic measurements are the top row and the warm measurements are on the bottom. For each array, dark measurements for 2, 12 and 100 second frametimes are shown. Each panel displays the median level of the bias after an estimate of the sky contribution was removed.
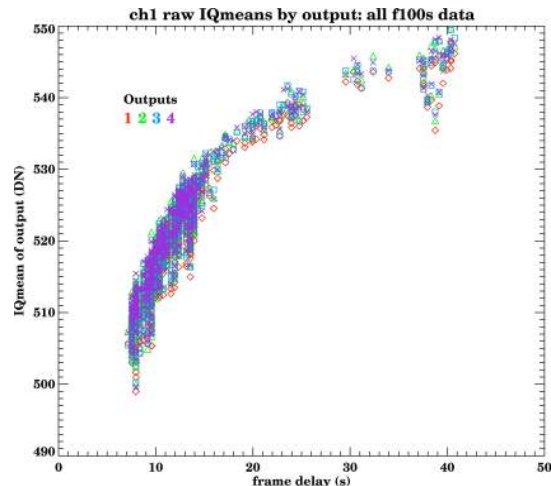
Figure 6. Bias variation as a function of delay time between frames for 3.6 μm 100 second frames. The mean of the raw frames per readout channel is plotted. Note that all four readouts have a similar behavior with the bias increasing with longer delay time. The functional shape is quite similar to the cryogenic effect, but the magnitude of the variation is much greater.

3.2 History dependant bias variation ("First-Frame" Effect)

In addition to the stable bias pattern, the bias of the Fowler sampled images also depends on the interval from the last data collection and the type of frame that was taken. The effect also has a second order dependency on the type and interval from previous frames, but the first order correction is sufficient for science purposes. For any given observation, the first frame has the largest interval from the proceeding frame and the bias variation is largest for larger intervals, hence the nickname "First-frame" effect. For the cryogenic mission, this history dependent variation was measured in the lab prior to flight using shutter closed measurements. The character of this variation is very different in the warm mission and the cryogenic lab calibration no longer applies. An on-orbit warm calibration of this effect is in progress using skydark frame data taken with a wide variety of intervals. As in the cryogenic mission, the history dependent variation consists of a DC offset, a column wise offset and a per-pixel offset with the per-pixel offset being much smaller than the first two contributions. Figure 6 displays the magnitude of the effect for 100 second 3.6 μm frames. For both channels, the effect is ~10× that of the cryogenic mission. As in the cryogenic effect, it appears to be repeatable; that is, you produce the same magnitude and pattern of the bias if you observe with the same cadence. As the effect is more significant in the warm mission, removal of it is a limiting factor for science observations that require high sensitivity for low surface brightness features such as investigations of galactic halos and intracluster light.

3.3 Linearity

Most surprisingly to the IRAC instrument team, the linearity correction for each array is quite different than the cryogenic solution. We had expected almost no variation at 4.5 μm as the applied bias across the detector is the same as in the cryogenic mission and had not anticipated that the variation at 3.6 μm (shown in Fig. 7) would be very significant. Both arrays are significantly non-linear in response when compared to the cryogenic mission. The linearity solution was determined from on-orbit data as was done for the cryogenic mission using a field sampled at a variety of frametimes and with a range of sources of known brightness. A quadratic solution is still applied for both channels but the linearity coefficient has increased from -1.9×10^{-6} to -3.5×10^{-6} at 3.6 μm and from -2.7×10^{-6} to -4.1×10^{-6} at 4.5 μm. As a result of the arrays being more non-linear, the effective well depth for each channel has been reduced by ~33% from 40,000 DN to 33,000 DN. In terms of source brightness, warm IRAC saturates at 323 and 364 mJy × s at 3.6 and 4.5 μm, respectively, for sources that are centered on an image pixel and a given observation frametime. Despite the more significant non-linearity, fluxes below saturation are correct to better than 1% just as in the cryogenic mission. The linearity solution for the observations before the final setpoint determination is less certain. Currently, the initial characterization linearity solution is applied to the data taken while the temperature is floating. Since the array bias is the more important variable in determining linearity, this solution should be reasonable, but not strictly correct as warm tests have shown that the linearity is also a function of temperature. Unfortunately, there is not enough data for sources of known brightnesses in the 12 August – 18 September 2009 time interval with which to construct an independent linearity
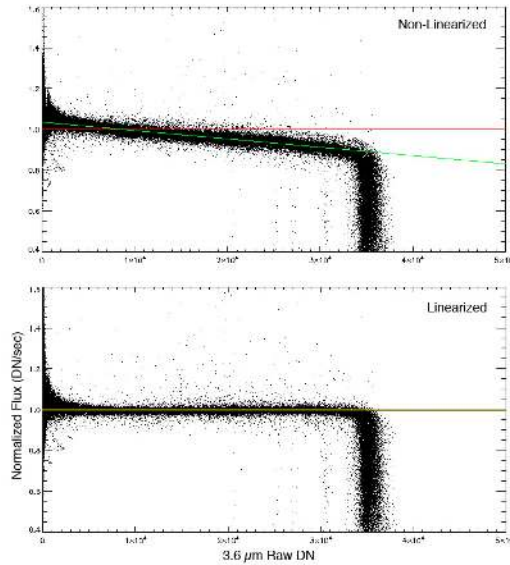
Figure 7. Warm linearity solution at 3.6 μm. The upper panel shows the raw DN compared to the true DN/s for each source in the SERVS field. The true DN/s are known from cryogenic observations of this field. The green line is the linearization solution and the bottom panel shows the linearized data. At about 33,000 DN, the linearization starts to fail which sets the effective well depth.

solution. Judicious scheduling during this time period tried to schedule primarily faint source observations which are more robust to uncertainties in linearization.
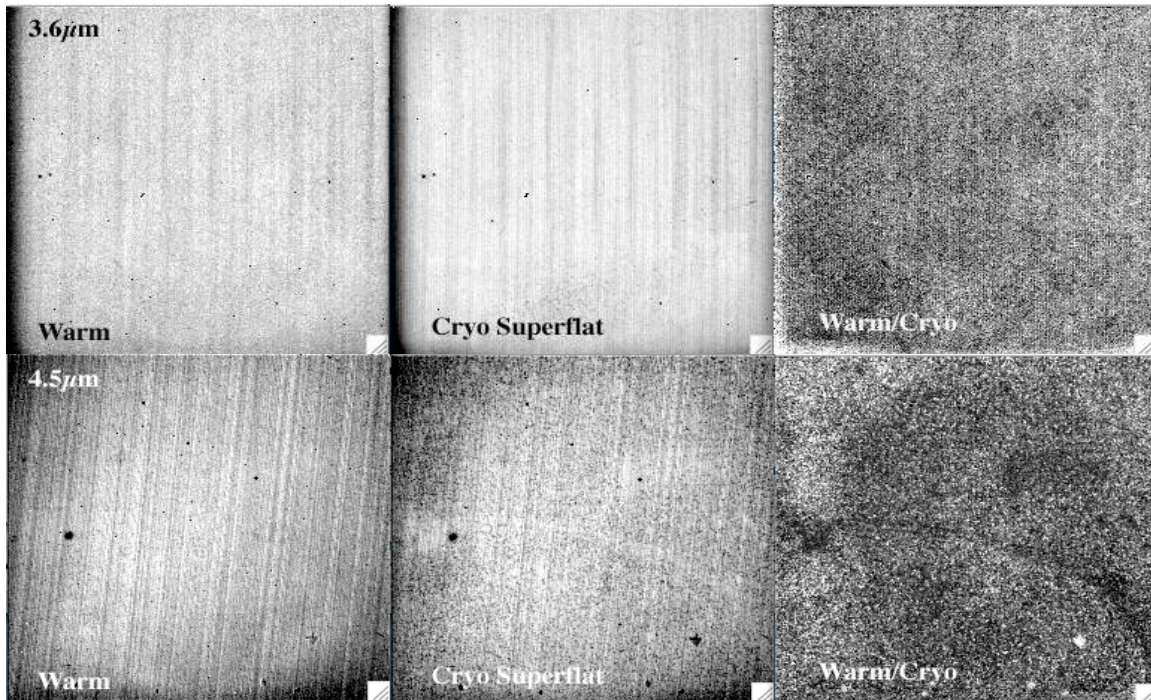
Figure 8. Warm (left), cryogenic (middle) and ratio of warm to cryogenic (right) flats at 3.6 μm (top) and 4.5 μm (bottom).

3.4 Flat-field (Gain map)

The warm data are flat-fielded using an analogous process as the cryogenic data. Observations of a high background region (field in the Ecliptic plane) are differenced with the low background skydarks and the per-pixel gain

normalization of each array is determined from a super flat-field determined from all the available calibration data as the flat-field does not vary with time to within our ability to measure it. Figure 8 displays the warm and cryogenic flat-fields. The precision of the warm flat-fields is 0.3% at 3.6 μm and 0.15% at 4.5 μm which is comparable to the precision of the cryogenic flats as we front loaded the calibration of the warm data in an effort to achieve comparable quality to meet the expectations of the science community. The warm flats are quite similar to the cryogenic flats with most pixels agreeing to about 1% and the largest discrepancies being 4%. The warm flats have similar large scale structure as the cryogenic flats except for the crescent feature in the cryogenic 4.5 μm flat which has disappeared in the warm flat.

3.5 Absolute calibration

The warm data are calibrated using the same methodology[11] as the cryogenic data. A set of nine primary calibrators are observed every two weeks with a rotating set of two secondary calibrators observed every downlink (usually about every 24 hours). The photometry of the primary calibrators are corrected for aperture size, array location-dependent photometric variations and pixel-phase response (the latter two effects are described in the next two subsections) and compared to the photometry for those calibrators from the cryogenic mission. The warm calibration factors which convert pipeline processed DN/s to surface brightness in MJy/sr are determined from the ratio of warm photometry to cryogenic photometry and scaling of the cryogenic flux conversion factors to account for that ratio. As previously mentioned, three sets of warm flux conversions are shown in Table 2. The flux conversion post final setpoint continues to be revised as we accumulate calibration star measurements. The uncertainty in calibration is 4.3% and 4.4% at 3.6 and 4.5 μm, respectively. The uncertainty in warm calibration compares favorably to the 3% uncertainty of the cryogenic mission and will improve as we accumulate better statistics. As in the cryogenic mission, 1.5% of the uncertainty is due to the absolute reference uncertainty in the fundamental calibrators, Vega and Sirius[11].

3.6 Pixel-phase correction

The photometry of sources imaged by the InSb arrays is a function of where the source centroid is relative to the center of a pixel[12]. This variation with pixel-phase is a manifestation of the non-uniform response of the pixels. In the cryogenic mission, the effect was about 4% peak-to-peak at 3.6 μm with the flux decreasing away from pixel center and was corrected using a linear function of distance from array center. At 4.5 μm, the effect was less than 1%, but certainly contributed to the scatter in photometry. For high precision photometric observations of exoplanets and other bright sources, the pixel-phase effect was the limiting factor in photometry for the cryogenic mission. As exoplanet science is a key component of the warm mission, a set of dedicated calibration observations for the pixel-phase were done as part of the initial characterization and calibration and were redone as part of the recalibration for the final setpoints. The observations were designed to produce pixel-phase maps with an accuracy of 0.1% for 0.1 pixel phase sampling.

The time spent in these calibrations was warranted, as the pixel-phase effect is much more extreme in warm data, 9% peak-to-peak at 3.6 μm and 4.7% peak-to-peak at 4.5 μm. Figure 9 displays the results of these calibrations. The peak response for pixels in each channel is slightly off center and the response drops towards the edges as a function of both x and y displacement. The effect is well fit by the product of Gaussians in Δx and Δy. The pixel at the pointing center for each full and subarray field of view were mapped as well as a coarser map around each pointing center. In addition, observations used to check the instrument focus were combined to produce an array average pixel-phase correction. In detail, the corrections for each pixel differ by more than the uncertainty in the fit parameters, but for each pixel studied and the array as a whole, the two-dimensional Gaussian is a good model for the effect and the array average corrects data to better than 0.2%. A reanalysis of cryogenic data has shown that the Gaussian model is a good representation of the pixel-phase correction at 3.6 μm; no definitive statement can be made about the cryogenic pixel-phase effect at 4.5 μm with the available data.

Correcting for the pixel-phase effect is significant for calibration and photometry of warm IRAC data. Previously published values of the flux conversion for the pre-final setpoint phases of the warm mission used a different convention for the normalization of the pixel-phase effect. In prior analysis, the pixel-phase effect was normalized to unity at peak response producing errors of ~4% and ~2% if no pixel-phase correction was applied to an ensemble of data. The flux conversions in Table 2 use the more standard convention of the pixel-phase being normalized to the map average.

3.7 Array location-dependent photometric correction

In addition to the photometry depending on where a source centroid lies relative to the center of a pixel, the photometry for blue sources (anything not as red as the Zodiacal light used to flat-field the images) depends on the position of the
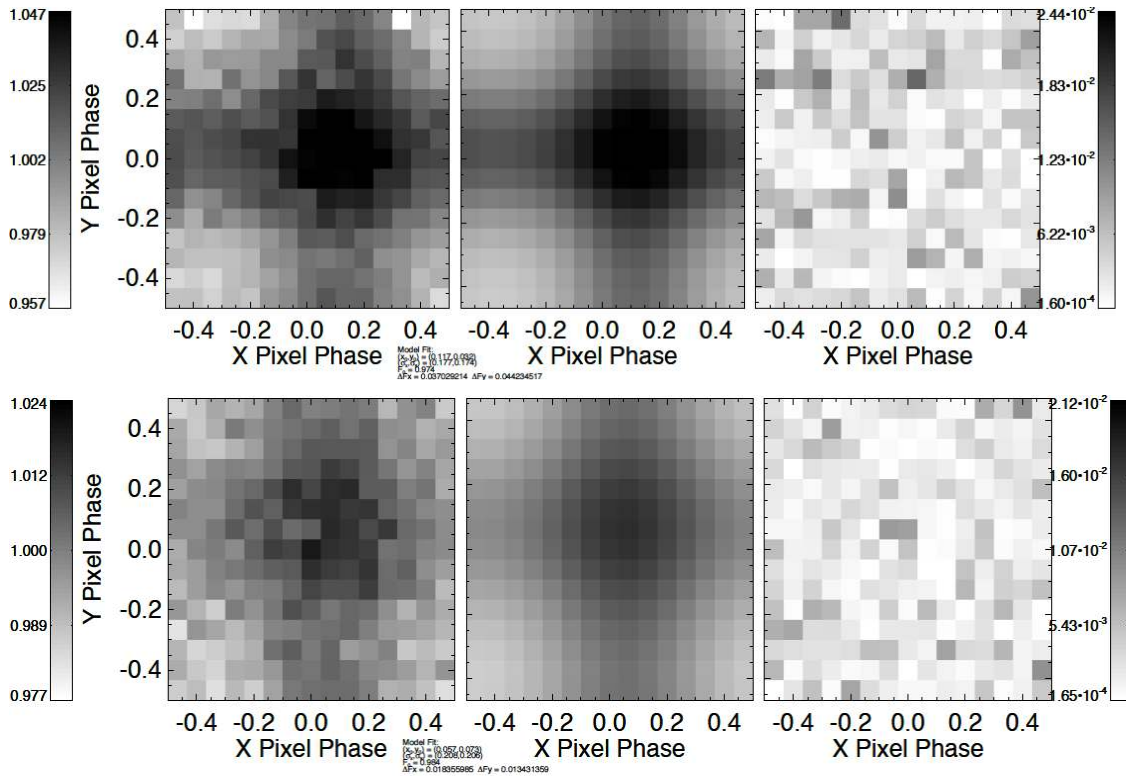
Figure 9. Binned relative photometry (left), pixel-phase fit (middle) and fit residuals (right) from the pixel-phase calibration at 3.6 μm (top) and 4.5 μm (bottom). The data and fits displayed are the array average sets.
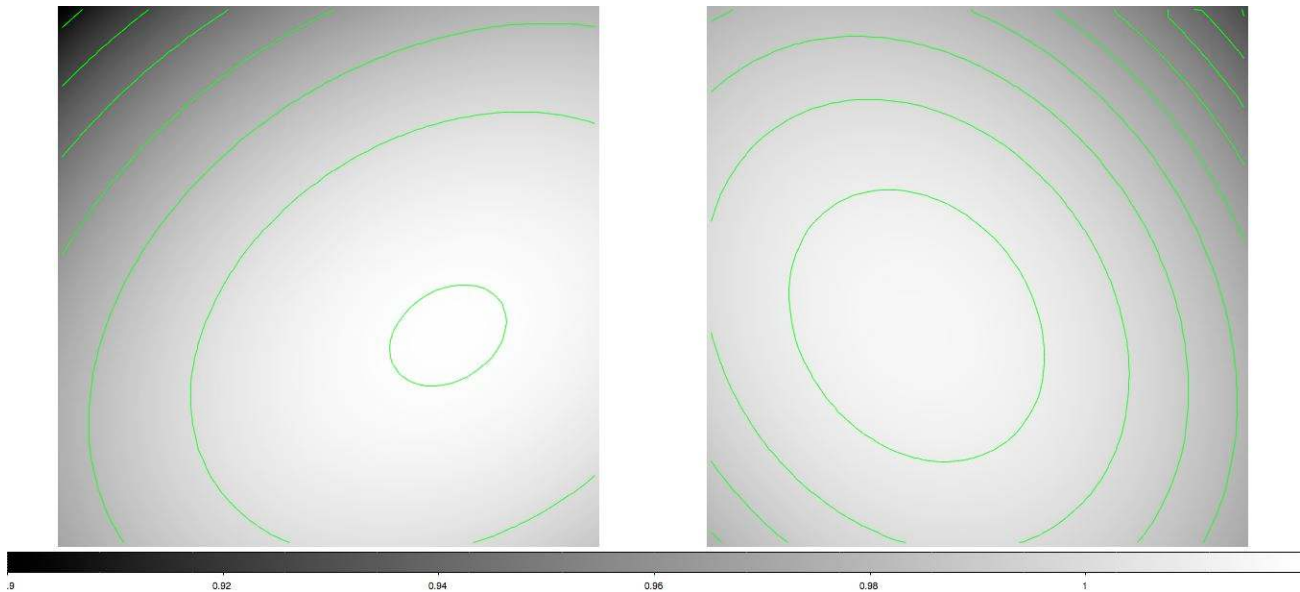

Figure 10. Maps of the array location dependent photometric correction at 3.6 μm (left) and 4.5 μm (right).

source centroid on the array[12,13]. This variation is a consequence of the variation in angle of incidence of light through the bandpass filters for different parts of the array. The sense of the correction is that sources appear to be brighter at the edges of the array. While the shift in response curves across the array does not entirely account for the magnitude of the observed effect, it is primarily optical in nature. Not surprisingly, the warm maps as shown in Figure 10 are very similar to the cryogenic maps with peak-to-peak variations of 6% at 3.6 μm and 8% at 4.5 μm with most of the array being within 2% of the center value (74% of the array at 3.6 μm and 60% of the array at 4.5 μm).
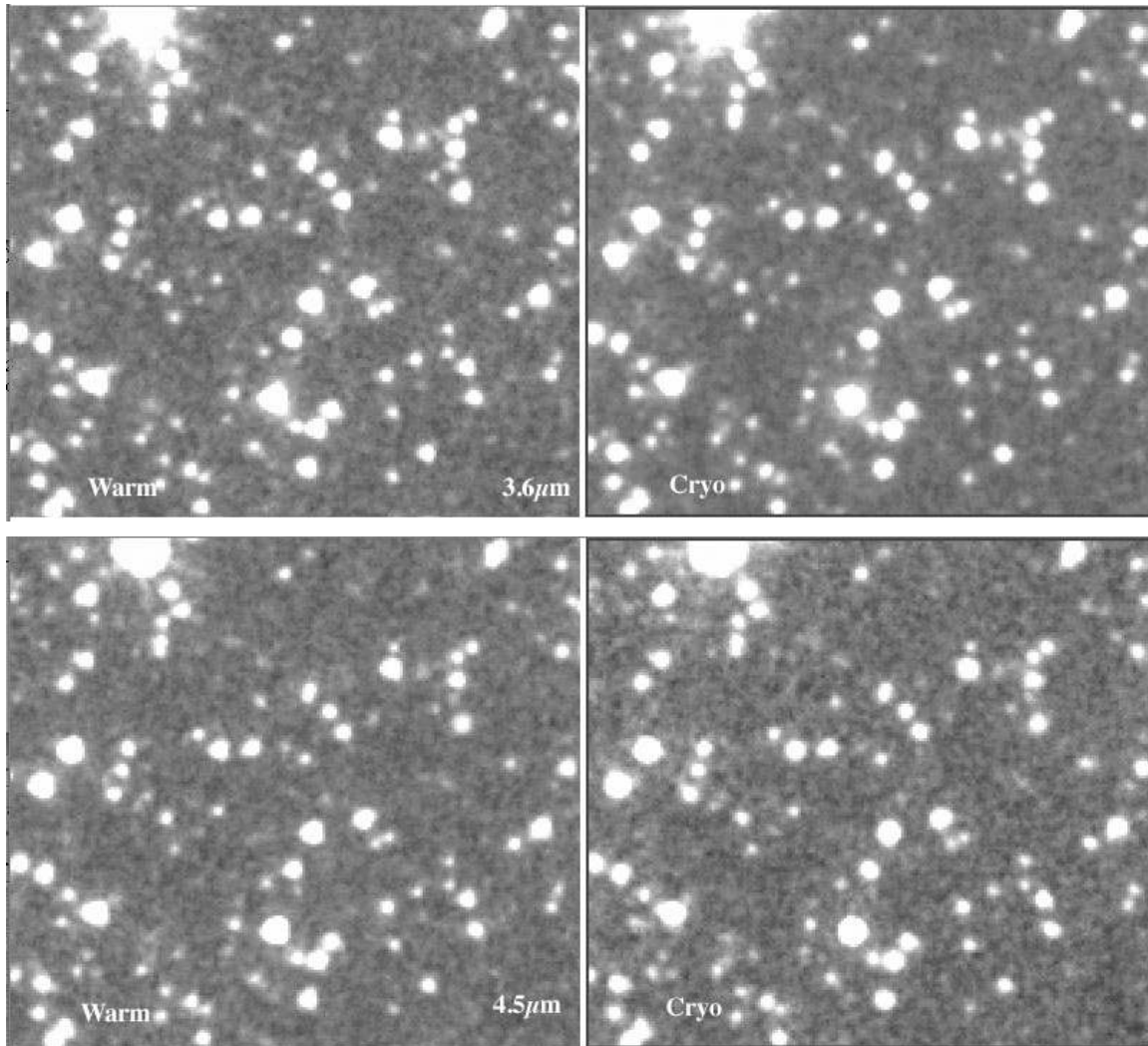
Figure 11. Comparison of 3 hours of integration of a field in the extended Groth Strip at 3.6 (upper) and 4.5 (lower) μm during the warm mission (left panels) and cryogenic (right). The warm data is a single epoch while the cryogenic data is the coaddition of three separate epochs which explains the slight rounder PSFs in the cryogenic mosaics.

4. IMAGE QUALITY AND ARTIFACTS

Figure 11 displays equivalent deep images from the warm and cryogenic missions. They are very similar with the 3.6 μm warm imaging appearing slightly noisier than its counterpart. Figure 12 displays the noise levels for 100 second integrations of a low background field. The 3.6 μm data is ~12% noisier while the 4.5 μm data is comparable to the cryogenic data. The noise measurements have about a 10% uncertainty and in general, the noise of an observation is a strong function of the background confusion and the data taking sampling. The warm noise measurements were made by measuring the dispersion of the pixel stacks for seven repeats of 100 second frames at three dither positions. Pixels containing sources and radhits were omitted before determining the dispersion. Warm IRAC has comparable but slightly worse sensitivity than cryogenic IRAC for deep imaging. For bright sources, signal-to-noise is photon limited. The relative sensitivities in the Poisson limit are
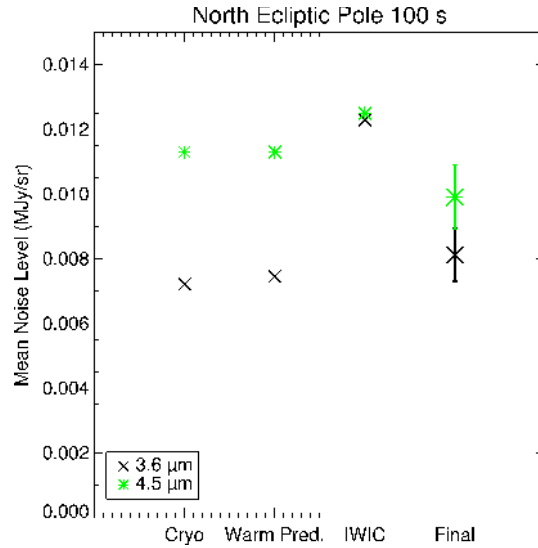
Figure 12. Noise measurements for one 100 second integration. The cryogenic values are from the SENS-PET sensitivity estimator, the warm prediction is determined from the cryogenic values with a 10% increase in read noise. The IWIC values are the measurements for the initial warm characterization and the final measurements are from the final setpoint calibration.

$$\sqrt{\frac{G_w \times C_c}{G_c \times C_w}},\tag{1}$$

where $G_{w,c}$ are the warm and cryogenic gains and $C_{w,c}$ are the warm and cryogenic flux conversions. The warm gains are 3.7 e⁻ per DN, while the cryogenic gains are 3.3 and 3.7 e⁻ per DN, at 3.6 and 4.5 μm. For the final setpoints, the warm sensitivities in the photon dominated limit are ~2% lower than cryogenic at both wavelengths.

IRAC exhibits the same photometric stability for high precision staring observations as in the cryogenic mission. Residuals in the characterization of the pixel-phase effect are the limiting factor in reaching photon-limited signal-to-noise. Several authors[14,15] have produced light curves with photon-limited precision, but there is some indication that the multiple epochs reduce the noise as $\sim N^{0.4}$, where N is the number of epochs coadded and binning over timescales of more than an hour (the period of the pointing wobble that produce the photometric variation) may also not achieve the $N^{0.5}$ reduction in noise. Conservatively, a signal-to-noise of

$$0.7 \times \sqrt{\frac{FtG}{C}} \times N^{0.4} = [20.3, 18.8] \times \sqrt{Ft} \times N^{0.4},\tag{2}$$

where F is the source flux in mJy, t is the integration time in seconds, G is the gain, C is the flux conversion and N is the number of samples averaged, is readily attainable. Figure 13 displays the photometry of a staring mode calibration and the ability to reduce noise by coaddition.

Compared to cryogenic data, the image artifacts in the warm data are more benign. There is no muxbleed or the associated multiplexer striping that was apparent for very bright sources. The very long term residual images at 3.6 μm that survived power cycles no longer occur. As a result, we do not anneal the arrays to mitigate residual images. The two image artifacts that are still present are more complicated standard residual images and a more complex column pulldown.

4.1 Residual images

The behavior of residual images for warm IRAC is unusual. While the long term residuals do not occur, there are significant residuals which last hours. What is surprising is that very bright sources (sources with a high fluence) on the arrays leave very small residuals. Sources as bright as -2.3 magnitudes at 3.6 μm were observed using 100 second images on the array and left only a small diffuse residual in subsequent frames. Apparently, there is a maximum cutoff
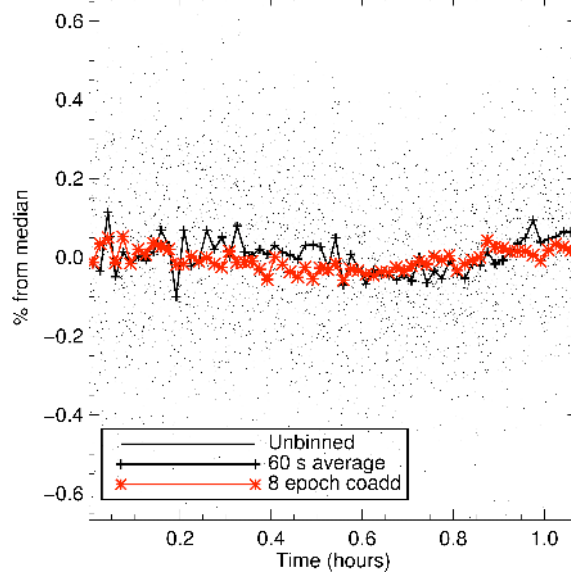
Figure 13. High signal-to-noise light curve of HD 157460. The points are the corrected individual photometry, the plus signs are the 60 second binned time series and the red curve is the coaddition of eight epochs of the 60 second binned time series.

for residual production which suggests some assisted depopulation of traps above a certain threshold. Due to this benign behavior, there are no restrictions on scheduling bright sources as there was for cryogenic obsevations. The residuals from intermediate brightness sources are more pronounced and there are more instances of slew latents which are produced when the arrays slew across a source without integrating. Examples of both types of residuals are shown in Figure 14. All warm residuals are mitigated with sufficient dithering.
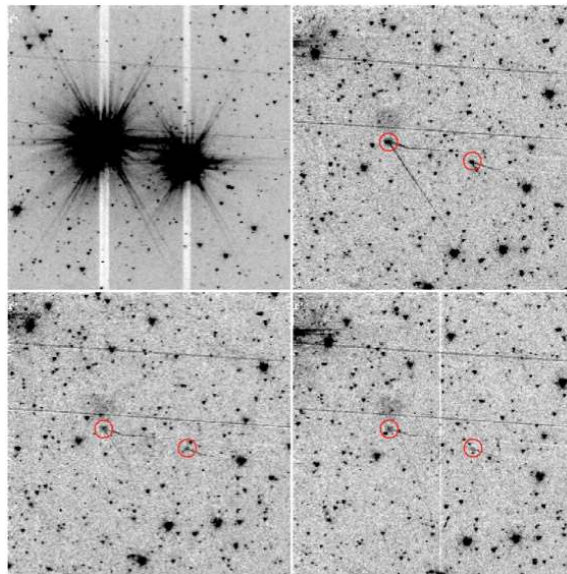

Figure 13. 3.6 μm, 12 second frames spaced about 30 seconds apart starting with an image of 5th and 7th magnitude stars (upper left), then subsequent dithers (upper right, lower left, lower right) showing the decay of residual images from those intermediate brightness stars. Also visible are slew latents (streaks across image above the stellar residuals) from brighter sources that happened to cross the array. Smaller and decaying slew latents are visible from the 5th and 7th magnitude stars.

4.2 Column pulldown

Column pulldown is a depression in the bias level of a column when a bright source is imaged on it. In the cryogen mission, column pulldown was well characterized by a DC offset above and different DC offset below the source. This

artifact was well corrected as part of the enhanced IRAC pipeline. In the warm mission, column pulldown is triggered by slightly fainter sources and has a more complex behavior. As shown in Figure 14, the pulldown is well modeled by
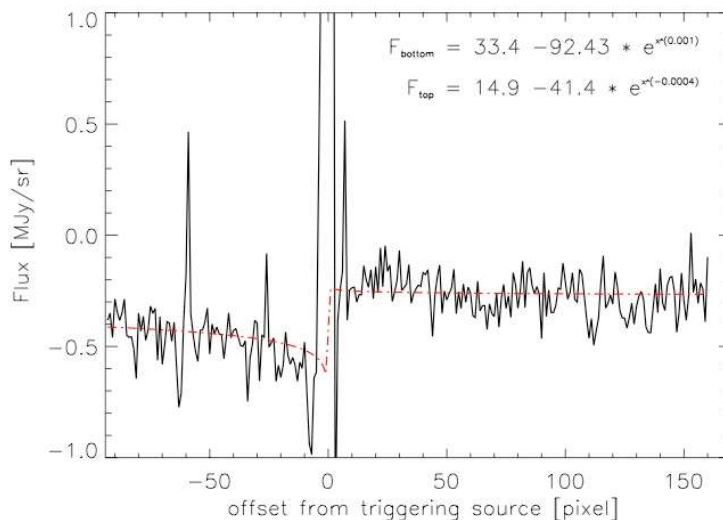

Figure 14. Example of fit to column pulldown. The pulldown corrected is the one triggered by the 7th magnitude star from Figure 13.

separate exponential fits above and below the source. The fit is determined iteratively from the difference of the artifact corrupted image and an estimate of the true sky derived using a Gaussian interpolate.

5. SUMMARY

The warm IRAC mission is producing science data of comparable quality to the cryogenic mission for the 3.6 and 4.5 μm channels and can continue to make profound scientific discoveries for many years. Figure 15 displays a representative science observation of a star forming region, DR 22. Apparent in this two color image are molecular outflows, protostars and dense molecular clouds seen in extinction. Array parameters have been optimized after an extended checkout phase. Warm data is at worst 10% less sensitive than cryogenic. The data are currently absolutely calibrated to 4%. Warm IRAC has the demonstrated the sensitivity necessary to detect galaxies at high redshift and the photometric stability to make high precision relative photometry observations of transits of approximately Earth sized planets around M stars and characterize the thermal phase curves of larger exoplanets.

REFERENCES

[1] Werner, M. N., Roellig, T. L., Low, F. J., Rieke, G. H., Rieke, M., Hoffmann, W. F., Young, E., et al., "The *Spitzer* Space Telescope Mission", ApJS, 154, 1-9, (2004).
[2] Rieke, G. H., Young, E. T., Engelbracht, C. W., Kelly, D. M., Low, F. J., Haller, E. E., Beeman, J. W., et al., "The Multiband Imaging Photometer for *Spitzer* (MIPS)," ApJS, 154, 25-29, (2004).
[3] Houck, J. R., Roellig, T. L., van Cleve, J., Forrest, W. J., Herter, T., Lawrence, C. R., Matthews, K., Reitsema, H. J., et al., "The Infrared Spectrograph (IRS) on the *Spitzer* Space Telescope", ApJS, 154, 18-24 (2004).

[4] Fazio, G. G., Hora, J. L., Allen, L. E., Ashby, M. L. N., Barmby, P., Deutsch, L. K., Huang, J.-S., et al., "The Infrared Array Camera (IRAC) for the *Spitzer* Space Telescope", ApJS, 154, 10-17, (2004).

[5] Hora, J. L., Fazio, G. G., Allen, L. E., Ashby, M. L. N., Barmby, P., Deutsch, L. K., Huang, J.-S., et al., "In-flight performance and calibration of the Infrared Array Camera (IRAC) for the *Spitzer* Space Telescope", Proc. SPIE 5487, 77-92, (2004).

[6] Cole, D. M, Carey, S. J., Surace, J. A., Glaccum, W. J., Ingalls, J., Krick, J., Lacy, M. D., Lowrance, P. J., et al. "Post-cryogenic Reanalysis of the Absolute Calibration of the Infrared Array Camera on the *Spitzer* Space Telescope", 7737-72, this proceeding, (2010).

[7] Carey, S., Surace, J., Lacy, M., Glaccum, W., Lowrance, P., Hora, J. L., and Willner, S. "Stability of the Infrared Array Camera for the *Spitzer* Space Telescope", Proc. SPIE 7010, 70102V-70102V-8 (2008).

[8] McMurty, C. W., Pipher, J. L., Forrest, W. J., "*Spitzer* space telescope: dark current and total noise prediction for InSb detector arrays in the infrared array camera (IRAC) for the post-cryogen era", Proc. SPIE 6265, 08, (2006).

[9] Storrie-Lombardi, L. J., et al., [The Science Opportunities of the Warm *Spitzer* Mission], AIP, 943, (2007).

[10] Chary, R., Surace, J., Carey, S., Berger, E. and Fazio, G., "GRB 090423: *Spitzer* observations of the z~8.3 burst", GRB Circular Service, 9582, (2009).

[11] Reach, W. T., Megeath, S. T., Cohen, M., Hora, J., Carey, S., Surace, J., Willner, S. P., Barmby, P., et al., "Absolute Calibration of the Infrared Array Camera on the *Spitzer* Space Telescope", PASP, 117, 978-990, (2005).

[12] Hora, J. L., Carey, S. J., Surace, J., Marengo, M., Lowrance, P., Glaccum, W. J., Lacy, M. Reach, W. T., et al., "Photometry Using the Infrared Array Camera on the *Spitzer* Space Telescope", PASP, 120, 1233-1243, (2008).

[13] Quijada, M. A., Marx, C. T., Arendt, R. G., Moseley, S. H., "Angle-of-incidence effects in the spectral performance of the infrared array camera of the *Spitzer* Space Telescope", Proc. SPIE 5487, 244-252, (2004).

[14] Hébrard, G. Desert, J.-M., Diaz, R. F., Boisse, I., et al., "Observation of the full 12-hour-long transit of the exoplanet HD80606b. Warm-Spitzer photometry and SOPHIE spectroscopy", arXiv:1004.0790, (2010).

[15] Deming, D., private communication.

Figure 15. 3.6 and 4.5 μm, two color image of the star forming region DR 22.